

This is the accepted manuscript made available via CHORUS. The article has been published as:

Vortex-antivortex proliferation from an obstacle in thin film ferromagnets

Ezio Iacocca and Mark A. Hoefer

Phys. Rev. B **95**, 134409 — Published 5 April 2017

DOI: [10.1103/PhysRevB.95.134409](https://doi.org/10.1103/PhysRevB.95.134409)

Vortex-antivortex proliferation from an obstacle in thin film ferromagnets

Ezio Iacocca^{1,2,*} and Mark A. Hoefer¹

¹*Department of Applied Mathematics, University of Colorado, Boulder, Colorado 80309-0526, USA*

²*Department of Physics, Division for Theoretical Physics,
Chalmers University of Technology, 412 96, Gothenburg, Sweden*

Magnetization dynamics in thin film ferromagnets can be studied using a dispersive hydrodynamic formulation. The equations describing the magnetodynamics map to a compressible fluid with broken Galilean invariance parametrized by the longitudinal spin density and a magnetic analog of the fluid velocity that define spin-density waves. A direct consequence of these equations is the determination of a magnetic Mach number. Micromagnetic simulations reveal nucleation of nonlinear structures from an impenetrable object including an applied magnetic field spot or a defect. In this work, micromagnetic simulations demonstrate vortex-antivortex pair nucleation from an obstacle. Their interaction establishes either ordered or irregular vortex-antivortex complexes. Furthermore, when the magnetic Mach number exceeds unity (supersonic flow), a Mach cone and periodic wavefronts are observed and can be well-described by the solution of the steady, linearized equations. These results are reminiscent of theoretical and experimental observations in Bose-Einstein condensates and further supports the analogy between the magnetodynamics of a thin film ferromagnet and compressible fluids. The nucleation of nonlinear structures and vortex-antivortex complexes using this approach enables the study of their interactions and effects on the stability of spin-density waves.

I. INTRODUCTION

Magnetization dynamics in thin film ferromagnets provide an exciting platform to study nonlinear wave phenomena. This is possible due to the exchange interaction that confers ferromagnetic order and wave dispersion, nonlinear effects such as anisotropy, and diverse mechanisms available to excite magnetization dynamics¹. In fact, coherent nonlinear magnetization structures were observed many decades ago, such as domain walls and vortices². More recently, envelope solitons^{3,4}, dissipative droplets^{5–9}, and skyrmions^{10–13} have also been observed in these materials. Another class of nonlinear structure in thin film ferromagnets is a spatially periodic, superfluid-like texture or soliton lattice^{14–18} that is able to carry spin currents due to its nontrivial topology, opening new pathways to nonlinear phenomena and potential applications.

Recently, soliton lattices have been interpreted in the context of hydrodynamics^{18,19}. It was shown that the Landau-Lifshitz (LL) equation describing magnetodynamics can be exactly cast as dispersive hydrodynamic equations, reminiscent of those describing Bose-Einstein condensates (BECs)²⁰ and other superfluid-like media²¹. A more direct, exact connection between polarization waves in two-component BECs²² and magnetization dynamics has recently been identified^{23,24}. From the magnetic dispersive hydrodynamic formulation, it is possible to characterize soliton lattices as dynamic, uniform hydrodynamic states (UHs) or static, spin-density waves (SDWs) parametrized by a longitudinal spin density n and fluid velocity \mathbf{u} proportional to the spatial gradient of the magnetization's in-plane phase. By defining the magnetic analog of the Mach number from classical gas dynamics, M , subsonic and supersonic flow conditions can be identified. Interestingly, this magnetic

fluid velocity, due to ferromagnetic exchange coupling, exhibits broken Galilean invariance at the level of (linear) spin wave excitations¹⁸. Consequently, the physics are reference-frame-dependent. This is in stark contrast to the velocity-dependent dynamics of localized, topological textures that result from their inherent nonlinearity^{25,26}.

Intriguing dynamics result from the interaction between a soliton lattice and a finite-sized obstacle. Micromagnetic simulations¹⁸ showed that, in general, SDWs ($\mathbf{u} \neq 0$) at subsonic conditions, $M < 1$, flow in a stable, laminar fashion around a point defect whereas a Mach cone, wavefronts, and irregular vortex-antivortex (V-AV) pair nucleation takes place at supersonic conditions, $M > 1$. In the different regime of thick, homogeneous ferromagnets ($\mathbf{u} = 0$), “spin-Cerenkov” radiation was observed in the moving reference frame²⁷. In classical fluids, similar coherent structures can be nucleated from an obstacle. The conditions defining the onset of specific features usually depend on the flow velocity or, equivalently, the Mach number. At subsonic conditions, obstacles can nucleate vortices resulting in an unsteady wake^{28,29}. A common example is the von Kármán vortex street, characterized by a train of vortices of alternating circulation. This has been thoroughly studied as a function of the Reynolds number for viscous, incompressible fluids²⁸. At supersonic conditions for a compressible gas, a Mach cone can be generated as typified by a jet breaking the speed of sound.

In contrast, superfluids such as BECs exhibit important differences. Firstly, vortices are quantized due to irrotational flow and secondly, BECs are compressible and inviscid. Therefore, a Reynolds number is not defined in the sense of classical fluids. However, it has been suggested that an alternative superfluid Reynolds number can be defined from the onset of quantum vortex shedding³⁰. In fact, V-AV pair dynamics can occur in super-

fluids as their numerical nucleation³¹ and instability³² were demonstrated at subsonic conditions. Numerical studies also identified the existence of a von Kármán-like vortex street³³, which has been recently demonstrated experimentally³⁴. At supersonic conditions, Mach cones have been observed, both theoretically and experimentally, accompanied by wave radiation or wavefronts ahead of the obstacle^{35,36} and, at large M , steady, oblique dark solitons can be generated inside the Mach cone³⁷.

The similarity between the equations describing BECs and thin film ferromagnetic magnetodynamics suggests that the latter may support the many structures mentioned above, with the possibility of new phenomena owing to a ferromagnet's more complex geometry. The stability of SDWs in a finite, thin film ferromagnet may be impacted by V-AV nucleation. It is known that V-AV pairs in magnets can excite spin waves by diverse annihilation processes³⁸, e.g., V-AV interaction with other V-AVs, with defects, or with physical boundaries. To explore the existence, dynamics, and stability of nonlinear structures in thin film ferromagnets, we analytically and numerically study the interaction between a SDW and an impenetrable, finite sized obstacle or defect.

In this paper, we show that in the static, laboratory reference frame, trains of V-AV pairs nucleated by a sufficiently large obstacle exhibit stable, linear motion at subsonic conditions whereas irregular V-AV dynamics are observed at supersonic conditions. This is due to the V-AV translation imposed by the underlying fluid velocity and the interactions between vortices, leading to translational instabilities or even V-V and AV-AV rotation. In the moving reference frame with zero fluid velocity, V-AV pairs generally annihilate, leading to irregular dynamics. However, at supersonic conditions, V-AV pairs exhibit structure by describing an oblique path inside the Mach cone. Wavefronts are observed to nucleate ahead of the obstacle in both reference frames at supersonic conditions. For thin film ferromagnets with finite extent, the observed nonlinear structures are transient as the system relaxes to an energy minimum. These results are not only relevant for the stability of a SDW but also represent a cornerstone to study V-AV complexes and their interaction with other nonlinear structures. More generally, our work provides an avenue to study proliferation of topological textures in magnetism. For example, recent numerical results have demonstrated the generation of skyrmions by spin-transfer torque from anisotropic obstacles³⁹, similar to the linear V-AV vortex motion we show below.

The paper is organized as follows. Section II summarizes the hydrodynamic formulation of the Landau-Lifshitz equation. The magnetic dispersive hydrodynamic equations obtained in section II are compared to the equations describing the mean field dynamics of BECs and two-component BECs in section III. In section IV, we use a linearized analysis to predict some properties of the patterns supported by the dispersive hydrodynamic flow past an obstacle. We also use analo-

gies to classical and superfluids to identify common flow patterns. Section V describes the results obtained from micromagnetic simulations. Finally, we provide our concluding remarks in section VI.

II. DISPERSIVE HYDRODYNAMIC FORMULATION

Following the formulation outlined in Ref. 18, the magnetization dynamics of a thin film ferromagnet with planar anisotropy can be conveniently described by the nondimensionalized LL equation

$$\frac{\partial \mathbf{m}}{\partial t} = -\mathbf{m} \times \mathbf{h}_{\text{eff}} - \alpha \mathbf{m} \times \mathbf{m} \times \mathbf{h}_{\text{eff}}, \quad (1)$$

with an effective field given by

$$\mathbf{h}_{\text{eff}} = \Delta \mathbf{m} - m_z \hat{\mathbf{z}} + h_0 \hat{\mathbf{z}}, \quad (2)$$

including, respectively, the ferromagnetic exchange field, local (zero-thickness limit) dipolar field, and a perpendicular external field. The dispersive hydrodynamic equations are obtained by inserting the transformation to Hamiltonian variables⁴⁰

$$n = m_z, \quad \mathbf{u} = -\nabla \Phi = -\nabla [\arctan(m_y/m_x)], \quad (3)$$

into Eq. (1), where $|n| \leq 1$ is the longitudinal spin density ($|n| = 1$ corresponds to the vacuum state) and \mathbf{u} is the irrotational fluid velocity. First, we exactly solve for $\partial \Phi / \partial t$ and obtain

$$\begin{aligned} \frac{\partial \Phi}{\partial t} = & -(1 - |\mathbf{u}|^2)n + \frac{\Delta n}{1 - n^2} + \frac{n|\nabla n|^2}{(1 - n^2)^2} \\ & + h_0 - \frac{\alpha}{1 - n^2} \nabla \cdot [(1 - n^2)\mathbf{u}]. \end{aligned} \quad (4)$$

The gradient of Eq. (4) and the equation for n are

$$\frac{\partial n}{\partial t} = \nabla \cdot [(1 - n^2)\mathbf{u}] + \alpha(1 - n^2) \frac{\partial \Phi}{\partial t}, \quad (5a)$$

$$\begin{aligned} \frac{\partial \mathbf{u}}{\partial t} = & \nabla [(1 - |\mathbf{u}|^2)n] - \nabla \left[\frac{\Delta n}{1 - n^2} + \frac{n|\nabla n|^2}{(1 - n^2)^2} \right] \\ & - \nabla h_0 + \alpha \nabla \left[\frac{1}{1 - n^2} \nabla \cdot [(1 - n^2)\mathbf{u}] \right]. \end{aligned} \quad (5b)$$

These are an exact transformation of the LL equation, Eq. (1), and fully describe the magnetization dynamics.

The ground-state solutions of Eqs. (5a) and (5b) are static magnetization textures known as spin-density waves (SDWs), such that

$$\frac{\partial \Phi}{\partial t} = \Omega = -(1 - \bar{u}^2)\bar{n} + h_0 = 0 \quad (6)$$

and the longitudinal spin density and fluid velocity, $(n, \mathbf{u}) = (\bar{n}, \bar{u}\hat{\mathbf{x}})$, are constants. This implies that the SDW can have a constant out-of-plane tilt and a periodic, in-plane spatial rotation of the azimuthal angle Φ .

For simplicity, we consider a non-negative fluid velocity along $\hat{\mathbf{x}}$, i.e., $\bar{u} > 0$.

The static condition Eq. (6) at a finite field corresponds to the ground state SDW conditions imposed by magnetic damping. If by some means $\Omega \neq 0$ in Eq. (6), e.g., by an abrupt jump in the field h_0 to another value h_1 , the associated dynamic solutions are considered UHSs¹⁸ that undergo a slow relaxation to a SDW. This relaxation process for $\bar{n}(t)$ maintains constant \bar{u} and can be computed by assuming spatial uniformity in Eqs. (5a) resulting in the temporal differential equation for the longitudinal spin density

$$\frac{d\bar{n}}{dt} = -\alpha(1 - \bar{u}^2)(1 - \bar{n}^2) \left(\bar{n} - \frac{h_1}{1 - \bar{u}^2} \right). \quad (7)$$

Upon integration, Eq. (7) yields the implicit relationship

$$\left[\frac{\left(\bar{n} - \frac{h_1}{1 - \bar{u}^2} \right)^2}{1 - \bar{n}^2} \right]^{1 - \bar{u}^2} \left(\frac{1 + \bar{n}}{1 - \bar{n}} \right)^{h_1} = C \exp \left\{ -2\alpha \left[(1 - \bar{u}^2)^2 - h_1^2 \right] \right\} \quad (8)$$

for $\bar{n}(t)$, where the constant C is determined from the initial density $\bar{n}_0 = h_0/(1 - \bar{u}^2)$. This expression composes an exponential decay of the density to the static state $\bar{n}(t) \rightarrow \bar{n}_1 = h_1/(1 - \bar{u}^2)$, $t \rightarrow \infty$ for any initial \bar{u} .

To study the dynamics originating from the interaction between a SDW and an obstacle, it is important to characterize small-amplitude perturbations of the SDW, described by the generalized spin wave dispersion relation

$$\omega_{\pm} = (2\bar{n}\mathbf{u} - \mathbf{V}) \cdot \mathbf{k} \pm |\mathbf{k}| \sqrt{(1 - \bar{n}^2)(1 - \bar{u}^2) + |\mathbf{k}|^2}, \quad (9)$$

where \mathbf{k} is the wave vector and \mathbf{V} is the velocity of an external observer or Doppler shift. This generalized dispersion relation reduces to the typical Galilean invariant, exchange-mediated spin wave dispersion in the vacuum limit $|\bar{n}| \approx 1$. However, Galilean invariance is broken in general¹⁸, leading to reference-frame-dependent physics.

From Eq. (9), one can derive the generalized spin wave phase and group velocities, respectively, v_p and v_g

$$v_{p,\pm} = \frac{\omega_{\pm}}{|\mathbf{k}|} \quad (10a)$$

$$= (2\bar{n}\mathbf{u} - \mathbf{V}) \cdot \hat{\mathbf{k}} \pm \sqrt{(1 - \bar{n}^2)(1 - \bar{u}^2) + |\mathbf{k}|^2}, \quad (10b)$$

$$v_{g,\pm} = \nabla_{\mathbf{k}} \omega_{\pm} = (2\bar{n}\mathbf{u} - \mathbf{V}) \cdot \hat{\mathbf{k}} \pm \frac{(1 - \bar{n}^2)(1 - \bar{u}^2) + 2|\mathbf{k}|^2}{\sqrt{(1 - \bar{u}^2)(1 - \bar{n}^2) + |\mathbf{k}|^2}}.$$

The long-wavelength limit $|\mathbf{k}| \rightarrow 0$ leads to coincident phase and group velocities, $v_p = v_g$, corresponding to the magnetic sound velocities imposed by the SDW

$$s_{\pm} = 2\bar{n}\bar{u} + \bar{V} \pm \sqrt{(1 - \bar{n}^2)(1 - \bar{u}^2)}, \quad (11)$$

where we have assumed $\mathbf{V} = -\bar{V}\hat{\mathbf{x}}$ and $\hat{\mathbf{k}} = \hat{\mathbf{x}}$ for simplicity.

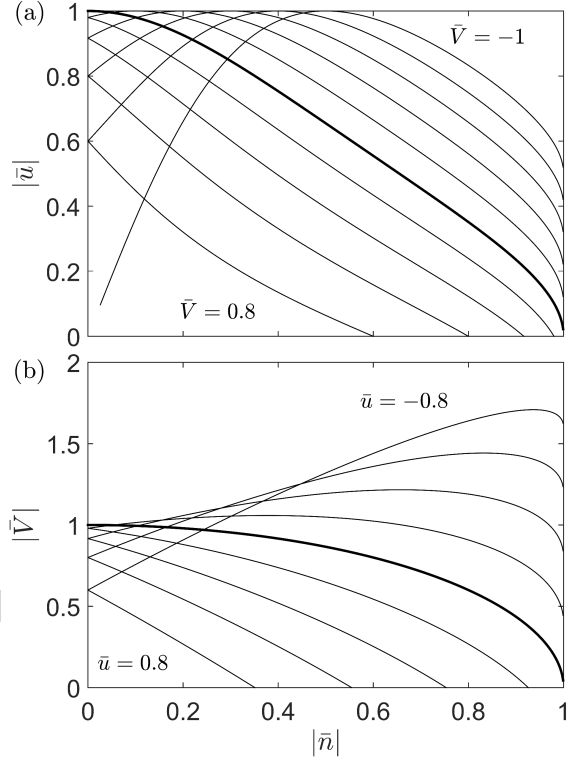


FIG. 1. Sonic curves calculated from Eq. (12) by varying (a) \bar{V} and (b) \bar{u} in steps of 0.2. The cases for (a) $\bar{V} = 0$ and (b) $\bar{u} = 0$ are emphasized by the thicker solid line, corresponding to Eq. (13).

Subsonic (counter-propagating waves) and supersonic (co-propagating waves) flow conditions can be identified from Eq. (11). In particular, the transition between these regimes, the sonic curve, occurs when $s_- = 0$ or $s_+ = 0$ in Eq. (11), resulting in

$$\bar{V}(\bar{V} + 4\bar{n}\bar{u}) = (1 - \bar{n}^2) - (1 + 3\bar{n}^2)\bar{u}^2. \quad (12)$$

Equation (12) represents the sonic surface for any \bar{V} , \bar{u} , and $|\bar{n}| < 1$, projections of which are shown in Fig. 1. Relatively simple expressions for Eq. (12) are available when we restrict to $\bar{V} = 0$ or $\bar{u} = 0$ (thicker lines in Fig. 1). Thus, we define the Mach numbers in these cases

$$M_u = \bar{u} \sqrt{\frac{1 + 3\bar{n}^2}{1 - \bar{n}^2}}, \quad M_V = \frac{\bar{V}}{\sqrt{1 - \bar{n}^2}}, \quad (13)$$

respectively, so that $M = 1$ corresponds to Eq. (12).

III. BOSE-EINSTEIN CONDENSATE LIMIT OF THE DISPERSIVE HYDRODYNAMIC EQUATIONS

The hydrodynamic equations governing the mean field dynamics of a BEC can be obtained as a limiting case of the magnetic, dispersive hydrodynamic equations,

Eqs. (5a) and (5b). For this, one should consider the nearly perpendicular, small velocity, long-wavelength, and low-frequency expansion

$$n = 1 - \epsilon\rho, \quad \mathbf{u} = \left(\frac{1}{2}\epsilon\right)^{1/2} \mathbf{v},$$

$$\tilde{\mathbf{x}} = \left(\frac{1}{2}\epsilon\right)^{1/2} \mathbf{x}, \quad \tilde{t} = \epsilon t, \quad U = \epsilon h_0, \quad (14)$$

where $0 < \epsilon \ll 1$ measures the magnetization deviation from the perpendicular vacuum state. Inserting this expansion into Eqs. (5a) and (5b) while keeping only the leading order terms and setting $\alpha = 0$ results in

$$\frac{\partial \rho}{\partial \tilde{t}} + \tilde{\nabla} \cdot (\rho \mathbf{v}) = 0, \quad (15a)$$

$$\frac{\partial \mathbf{v}}{\partial \tilde{t}} + (\mathbf{v} \cdot \tilde{\nabla}) \mathbf{v} + \tilde{\nabla} \rho = \frac{1}{4} \tilde{\nabla} \left[\frac{\tilde{\Delta} \rho}{\rho} - \frac{|\tilde{\nabla} \rho|^2}{2\rho^2} \right] - \tilde{\nabla} \mathcal{U} \quad (15b)$$

a non-dimensional form of the conservative, hydrodynamic equations of a repulsive BEC with trapping potential $V(\tilde{\mathbf{x}})$ (see, e.g., Ref. 20). From this analogy it follows that the “healing length” defined in BEC as the transition distance between two states with dissimilar density is simply given by the spatial scaling in ferromagnetic materials, i.e., the exchange length in the case of planar ferromagnets¹⁸.

BECs can lose superfluidity when its interaction with an obstacle results in the generation of small-amplitude waves²⁰. This can be described in terms of the Landau criterion for superfluidity, which invokes Galilean invariance to find the conditions where spontaneous wave generation is energetically unfavorable. For a BEC described by Eq. (15), the Landau criterion is $|\mathbf{v}| < s$ where $s = \sqrt{\rho}$ is the BEC long wave speed of sound.

For BECs, the Landau criterion and the Mach number are closely related. Both describe the conditions for subsonic to supersonic flow transitions. The Mach number for BECs is²⁰

$$M_{\text{BEC}} = \frac{|\mathbf{v}|}{\sqrt{\rho}}. \quad (16)$$

The sonic curve, $M_{\text{BEC}} = 1$, is the critical transition from subsonic to supersonic conditions and represents the breakdown of superfluidity, i.e., spontaneous wave generation is energetically unfavorable. It can be verified that the magnetic Mach numbers, Eq. (13), reduce to Eq. 16 for small deviation from vacuum, by inserting the transformation (14) into (13). Since the standard derivation of the Landau criterion utilizes Galilean invariance, it can *only* be applied to exchange-mediated, Galilean invariant spin waves in a perpendicularly magnetized thin film ferromagnet. Away from this regime, SDWs break Galilean invariance¹⁸. The more general identification of the subsonic to supersonic transition as the breakdown of superfluidity is the appropriate one for SDWs because the generalized spin wave dispersion (9) exhibits non-zero curvature for positive wavenumbers.

It is important to stress that Eqs. (15) are conservative, so that the connection between BECs and exchange-mediated spin waves is valid insofar as magnetic damping is neglected. However, because damping is typically weak $0 < \alpha \ll 1$, we can invoke conservative arguments to describe the dynamics and nucleated structures over sufficiently short timescales (proportional to α^{-1}) when a finite-sized obstacle is introduced.

A more general analog to the magnetic, dispersive hydrodynamic equations, Eqs. (5a) and (5b), can be found in two-component Bose-Einstein condensates, a class of spinor Bose gases²² that possess magnetic properties. In particular, Congy *et al.*²⁴ found that the polarization waves in a one-dimensional, two-component BEC can be described by approximate dispersive hydrodynamic equations coinciding exactly with the one-dimensional projection of Eqs. (5a) and (5b) when $\alpha = 0$. This suggests that observations in planar ferromagnets can be applicable to two-component BECs and showcases the effects of exchange coupling between spins or atoms with a finite magnetic moment. Magnetic damping carries energy away from a planar ferromagnet, at which point the analogy to a superfluid strictly breaks down.

Finally, we remark that there exists yet another exact mapping of the dispersive hydrodynamic magnetization equations (4), (5) (one-dimensional, $\alpha = 0$) to a continuum model of a hard core Boson gas^{41,42}.

IV. NUCLEATION OF NONLINEAR STRUCTURES IN FERROMAGNETIC THIN FILMS

Inspired by classical, incompressible fluids and BECs, we discuss the diverse nonlinear structures that can be nucleated from an impenetrable obstacle in a ferromagnetic thin film. We numerically confirm the main points of our discussion in the following Section V.

In the near vacuum regime, when the magnetodynamics limit to a BEC (cf. Sec. III), it is possible to qualitatively predict the resulting dynamics^{31–33,35–37}. In the subsonic regime, $M < 1$, quantized V-AV pairs are expected to be nucleated for sufficiently large diameter obstacles. This occurs because the obstacle gives rise to a local acceleration of the flow and the fluid velocity develops a transverse component, $u_y = \mathbf{u} \cdot \hat{\mathbf{y}} \neq 0$. Locally, the total fluid velocity reaches supersonic conditions, making the wake unsteady and periodically nucleating vortices. We stress that the global topology of the magnetic texture in an infinite film must remain constant, suggesting that only V-AV pairs can be nucleated. Consequently, a von Kármán vortex street composed of single vortices of alternating circulations is not favorable in ferromagnets although an analog utilizing V-AV pairs has been numerically³³ and experimentally³⁴ observed in BEC.

As V-AV pairs are nucleated, two types of interactions are possible. On the one hand, Vs and AVs are attractive and can annihilate by transferring their energy to spin

waves³⁸. On the other hand, when there is an underlying flow, a V-AV pair can form a stable entity exhibiting two types of dynamical behavior, which we describe in a qualitative fashion inspired by the well-known dynamics of vortices in classical incompressible fluids²⁹ and BECs^{31,32}. If each V-AV pair is decoupled from other V-AV pairs, the flow translates the V-AV pairs in a train²⁹, similar to the Kelvin motion of same-polarity V-AV pairs studied in planar ferromagnets with $\mathbf{u} = 0$ ⁴³. However, such a train of parallel V-AVs was numerically observed to be unstable for propagation according to the hydrodynamic equations (15) for a BEC³² and may accommodate sinuous or varicose modes, where a sinusoid describes the position of the V-AV pairs or the Vs and AVs in the train, respectively. When the V-AV pairs are sufficiently close to each other, V-V and AV-AV interactions can take place, leading to their rotation about a vorticity center²⁹. As we show in the next section, these dynamics are observed numerically in magnetic hydrodynamic flow past finite-sized obstacles.

In the supersonic regime, a distinguishable feature is a Mach cone corresponding to steady, small amplitude, long waves. The aperture angle of the Mach cone, referred to as the Mach angle μ , can be determined by assuming steady, small-amplitude, long-wavelength perturbations nucleated from the obstacle (see, e.g., Ref. 44). Because these are two-dimensional perturbations, we assume a wave vector $\mathbf{k} = k_x \hat{\mathbf{x}} + k_y \hat{\mathbf{y}}$ with $|\mathbf{k}| \ll 1$. Let us also assume that the fluid and external velocities have only $\hat{\mathbf{x}}$ components. The resulting *time-dependent* long-wavelength dispersion relation is just Eq. (9) keeping only the linear in $|\mathbf{k}|$ terms

$$\omega_{\pm} = (2\bar{n}\bar{u} + \bar{V}) k_x \pm \sqrt{k_x^2 + k_y^2} \sqrt{(1 - \bar{n}^2)(1 - \bar{u}^2)}. \quad (17)$$

The Mach cone is established as a steady state, thus we are interested in the relationship between k_x and k_y when $\omega_{\pm} = 0$. The Mach angle μ can be calculated by trigonometric identities as $\tan \mu = k_x/k_y$. Incorporating this transformation into Eq. (17) with $\omega_{\pm} = 0$ and squaring leads to

$$(2\bar{n}\bar{u} + \bar{V})^2 \sin^2 \mu = (1 - \bar{n}^2)(1 - \bar{u}^2). \quad (18)$$

Solving Eq. (18) for the cases $\bar{V} = 0$ and $\bar{u} = 0$ leads to the definition of μ_u and μ_V , respectively

$$\mu_u = \sin^{-1} \frac{\sqrt{(1 - \bar{n}^2)(1 - \bar{u}^2)}}{2|\bar{n}\bar{u}|} \leq \frac{\pi}{2}, \quad (19a)$$

$$\mu_V = \sin^{-1} \frac{\sqrt{1 - \bar{n}^2}}{\bar{V}} = \sin^{-1} \frac{1}{M_V} \leq \frac{\pi}{2}. \quad (19b)$$

Note that Eq. (19b) reduces to the Mach angle of a classical gas with Mach number M_V ⁴⁴. In contrast, Eq. (19a) is a more complex expression of \bar{u} and \bar{n} ; note that μ_u and μ_V are real-valued only for $M_{u,V} \geq 1$ ($M_{u,V} = 1$, $\mu_{u,V} = \pi/2$). The non-standard form of the Mach angle μ_u is another consequence of the broken Galilean invariance of the magnetic system.

In steady flow, nonlinear structures are expected to reside inside the Mach cone³⁷. Outside the Mach cone, a static, $\omega = 0$, structure can also be established. This linear wavefront, also referred to as Cerenkov radiation^{27,35}, features a wave vector with constant phase curves describing an approximate parabola around the obstacle. As outlined in Ref. 36, the constant phase curves can be described in polar coordinates (r, χ) defined as a function of the angle η , schematically shown in Fig. 2. This is achieved by assuming slowly modulated, stationary waves $\mathbf{k} = |\mathbf{k}|(\cos \eta \hat{\mathbf{x}} + \sin \eta \hat{\mathbf{y}}) = \nabla \theta$. From the static condition $\omega_{\pm} = 0$ in Eq. (17), it follows that

$$|\mathbf{k}|^2 = (2\bar{n}\bar{u} - \bar{V})^2 \cos^2 \eta - (1 - \bar{n}^2)(1 - \bar{u}^2). \quad (20)$$

This implies, for constant η , that larger fluid or observer velocities lead to shorter wavelengths. For time-independent \mathbf{k} and noting that $\nabla \times \mathbf{k} = 0$ due to irrotationality, it is possible to introduce a hyperbolic equation for k_x and k_y that can be solved by the method of characteristics³⁷. Integrating $\nabla \theta$ along a constant χ yields

$$\tan \chi = -\frac{\partial \omega / \partial k_y}{\partial \omega / \partial k_x}, \quad (21a)$$

$$|\mathbf{r}| = -\frac{\theta}{|\mathbf{k}| \cos \psi}, \quad (21b)$$

where ψ is the angle between \mathbf{r} and \mathbf{k} . For fixed phase θ , Eqs. (21a) and (21b) represent the solution of a constant phase curve, as schematically represented by the red line in Fig. 2. It is also possible to recast this solution in Cartesian components (x, y) . In the moving reference frame with $\bar{u} = 0$, $\bar{V} \neq 0$, the result coincides with that presented in Ref. 36. In the static reference frame $\bar{u} \neq 0$, $\bar{V} = 0$, we obtain by trigonometric identities and algebra

$$x = \frac{\theta \cos \chi}{|\mathbf{k}| \cos \psi} = \frac{\theta \cos \eta (\sin^2 \mu_u + 1 - 2 \cos^2 \eta)}{2\bar{n}\bar{u} (\cos^2 \eta - \sin^2 \mu_u)^{3/2}}, \quad (22a)$$

$$y = \frac{\theta \sin \chi}{|\mathbf{k}| \cos \psi} = -\frac{\theta \sin \eta (\cos^2 \eta - [\sin^2 \mu_u]/2)}{2\bar{n}\bar{u} (\cos^2 \eta - \sin^2 \mu_u)^{3/2}}. \quad (22b)$$

It must be noted that far away from the obstacle, when $|\eta| \rightarrow \pi/2$ and in the limit of long-wavelengths $|\mathbf{k}| \ll 1$, Eq. (21a) approaches the solution $\chi \rightarrow \mu$. Therefore, the wavefronts are asymptotically parallel to the Mach cone. Close to the obstacle, when $|\eta| \ll 1$, a series expansion yields the approximate parabolic wavefront profile

$$x \sim -\theta + y^2 \frac{(2\bar{n}\bar{u})^2 (1 - \sin^2 \mu_u)^2 (4 + \sin^2 \mu_u)}{|\theta| (2 - \sin^2 \mu_u)} \quad (23)$$

V. NUMERICAL RESULTS

The existence and dynamics of nonlinear structures hypothesized in Sec. IV for planar ferromagnetic thin films

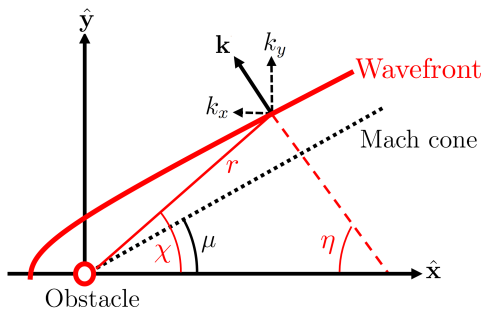


FIG. 2. (color online) Schematic representation of a wavefront constant phase line (red solid line), traced by $\chi(\eta)$ and $r(\chi, \eta)$. The wavefronts are asymptotically parallel to the Mach cone (black dashed line) far from the obstacle (red circle).

can be verified by micromagnetic simulations. We consider impenetrable obstacles with a circular cross section and diameter d . Due to broken Galilean invariance, we perform simulations in both the static and moving reference frames, as described below. It is important to point out that the continuous nucleation of topological structures requires an energy source, such as spin injection at a ferromagnetic boundary^{15,16}. In our simulations, we do not consider such an energy source per se. Rather, the stabilization of nonzero velocity \mathbf{u} —although static, $-(1 - n^2)\mathbf{u}$ is nevertheless a spin current¹⁸—is assumed to result from some external mechanism, analogous to the sustenance of a flowing classical fluid. The introduction of an obstacle is a perturbation to the system that imposes a new energy minimum. This leads to a transient regime where topological structures are nucleated as the total energy of the system is minimized. Therefore, we report and interpret the dynamics observed during such a transient from a dispersive hydrodynamic perspective.

A. Static reference frame, $\bar{u} \neq 0$ and $\bar{V} = 0$

We perform finite-difference integration of the LL equation using the GPU-accelerated micromagnetic package MuMax3⁴⁵. Although we report solutions of the nondimensional LL equation, Eq. (1), the parameters are consistent with Permalloy, e.g., saturation magnetization $M_s = 790$ kA/m, exchange stiffness $A = 10$ pJ/m³, and Gilbert damping $\alpha = 0.01$. To compare with theory, we consider only local dipolar fields (zero thickness limit) by incorporating a negative perpendicular anisotropy constant $K_u = -\mu_0 M_s^2/2$, where μ_0 is the vacuum permeability. With these parameters, space is normalized to the exchange length λ_{ex} and time to $1/(\gamma\mu_0 M_s)$, where γ is the gyromagnetic ratio. Typical values for these parameters are $\lambda_{\text{ex}} = 5$ nm, $1/(\gamma\mu_0 M_s) = 36$ ps, $\gamma = 28$ GHz/T.

An impenetrable obstacle is introduced as a localized (hyper-Gaussian), perpendicular field that forces $\bar{n} = 1$,

i.e., the vacuum state, in a limited area¹⁸. In fact, a perpendicular field acts as a potential body force on the fluid as shown in Eq. (5b). Alternatively, a magnetic defect or absence of magnetization also constitutes an impenetrable object. Similar results are obtained from both approaches, shown below in Fig. 4. As an initial condition, we impose a SDW given by $(\bar{n}, \bar{u} = 0.6)$ with $0 < \bar{n} < 1$ and guarantee its stability by both applying a homogenous, perpendicular magnetic field that satisfies Eq. (6) and defining a simulation domain of 317×156 that accommodates an exact number of SDW periods in the \hat{x} direction. The simulation is discretized into a 1024×512 mesh and we implement periodic boundary conditions along the \hat{x} direction and open or free-spin conditions in the \hat{y} direction. The simulation is evolved to the time $t = 112$. In order to prevent any nucleated structure from propagating through the periodic boundaries, we also implement a high damping region close to the edge of the simulation domain. Such an absorbing boundary does not compromise the stability of the initialized SDW. We emphasize that the choice of fluid velocity $\bar{u} = 0.6$ was made on the basis of computational speed. Other fluid velocities give similar results.

The observed nucleated nonlinear structures can be classified in the phase space spanned by the parameters \bar{n} and d , shown in Fig. 3(a), swept in steps of 0.1 and 1, respectively. First, we note that laminar flow (region O) is lost as the diameter of the obstacle increases, even in the subsonic regime (below the dashed line), indicating that the fluid velocity locally develops supersonic speed as it is accelerated around the obstacle. We have verified this fact numerically. The gray regions represent ordered V-AV pair nucleation. For a relatively narrow parameter space (region I), the V-AV pairs translate parallel to each other carried by the underlying flow, as shown in Fig. 3(b). In region II, the parallel V-AV trains are unstable³², Fig. 3(c). We note that the instability numerically observed for parallel V-AV pairs in BECs³² suggests that region I could eventually develop an instability for larger simulation domains and times. However, simulations in a domain twice as large 634×212 , evolved twice as long to $t = 224$ did not show evidence of such an instability. Finally, region III denotes irregular V-AV nucleation, as shown in Fig. 3(d). Here, V-V and AV-AV rotation is observed, schematically shown in Fig. 3(d) by the blue lines defining the V-V and AV-AV axis and blue arrows denoting the rotation. In all cases above, we observe that the separation between the V and AV in a pair increases as they translate away from the obstacle. This was also observed in additional simulations where a single V-AV pair was nucleated by a field pulse. Such a single pair moves with a velocity greater than $|\mathbf{u}|$ and develops a velocity transverse to \mathbf{u} . This is in contrast to constant V-AV motion in a uniform magnetic background⁴³. An in-depth study of V-AV motion on a textured background is worth of future investigation but lies outside the scope of the present paper.

Micromagnetic simulations were performed also in the

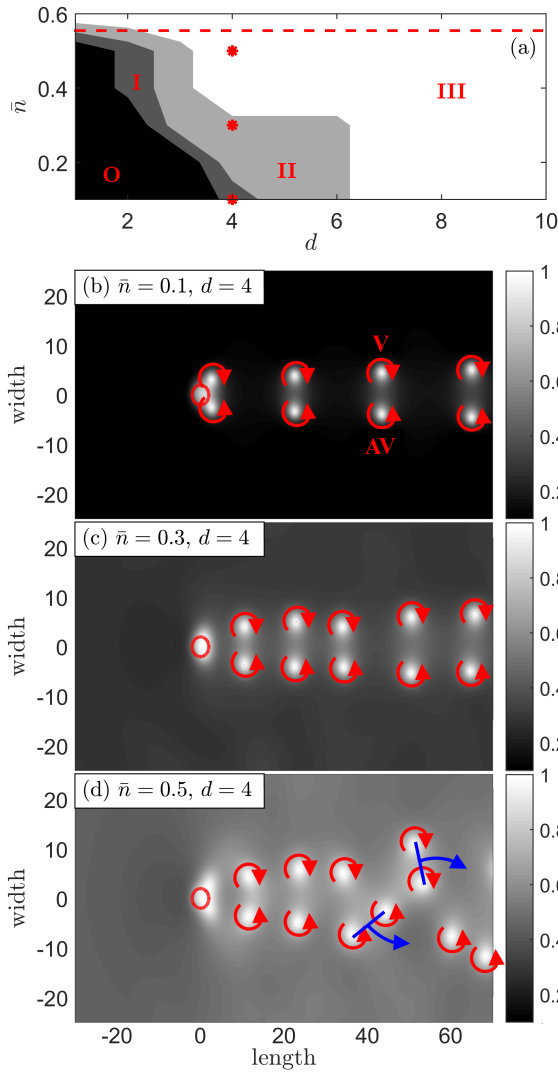


FIG. 3. (color online) (a) Phase diagram for V-AV nucleation and dynamics in the static reference frame. Region O represents laminar flow while the gray regions I-II (III) denote ordered (irregular) V-AV pair nucleation. Snapshots of the longitudinal spin density, n , exemplify each region showing V-AV pairs in (b) parallel (region I), (c) unstable mode (region II), and (d) irregular dynamics (region III), with corresponding conditions indicated by red asterisks in (a). The red arrows represent the vortices' circulation direction, with V and AV circulations indicated in (b). The blue lines and arrows schematically show the rotating trajectory of the V-V and AV-AV pairs in the irregular regime.

case where a magnetic void serves as an obstacle. The resulting \bar{n} vs d phase space is shown in Fig. 4(a) and qualitatively agrees with the phase diagram obtained with a localized field, Fig. 3(a). We note that in this case, the instability of the V-AV pairs train develops into a sinuous mode, Fig. 4(b). Furthermore, we observe a transition between region II and III, labeled region IV in Fig. 4(a), where we observe V-V and AV-AV nucleation reminiscent of von Kármán vortex streets numerically predicted

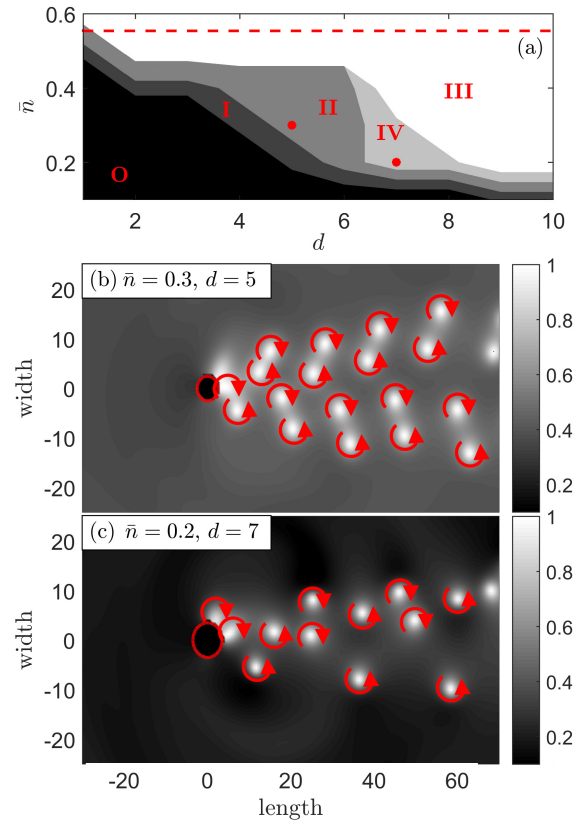


FIG. 4. (color online) (a) Phase diagram for V-AV nucleation and dynamics in the static reference frame considering a magnetic defect as an obstacle. The black region represents laminar flow while the gray regions (white region) denotes ordered (irregular) V-AV pairs nucleation. Regions I and II qualitatively agree with the dynamics observed in Fig. 3. Here, region II exhibits a sinuous mode (b), in contrast to Fig. 3. Additionally, a von Kármán-like vortex street is observed in region IV (c). We do not show regions I and III as they are similar to Figs. 3b and 3c, respectively.

and recently observed in BECs^{33,34}.

Irregular V-AV nucleation persists for supersonic conditions, when $M_u > 1$ [above the red dashed line in Fig. 3(a)]. Additionally, in this regime we also observe a well-defined Mach cone and the nucleation of wavefronts, Fig. 5. As discussed in Sec. IV, the Mach angle and curves of constant phase corresponding to wavefronts are given in Eqs. (19a) and (22), which describe the numerical results to good accuracy, as shown by red dotted lines in Fig. 5. Whereas the Mach angle defines a static boundary i.e., the Mach cone, the wavefronts lose energy through damping at the boundaries in our energy minimizing simulations. For this reason, the red dashed line outlining the wavefront in Fig. 5 is obtained by fitting θ and a horizontal shift from the obstacle. The wavelength $2\pi/k = \lambda = 19$ at $\eta = 0$ is well-described by Eq. (20) and is found to be within the same order of magnitude as the numerically calculated wavefront wavelengths throughout the simulation evolution $\lambda_{\text{sim}} = 12.21 \pm 2.1$. This

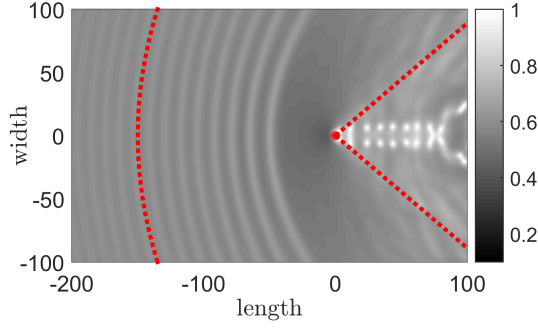


FIG. 5. (color online) Snapshot of the longitudinal spin density, n , in the static reference frame at a supersonic condition $(\bar{n}, \bar{u}) = (0.6, 0.6)$ and an obstacle of diameter $d = 6$. The Mach cone calculated from Eq. (19a) and the wavefront calculated from Eq. (22) are shown by red dashed curves.

agreement is possible due to the fact that damping in a SDW is balanced by the applied perpendicular field, so that the equations are effectively conservative and the concepts used for BEC are approximately applicable.

B. Moving reference frame, $\bar{u} = 0$ and $\bar{V} \neq 0$

In the moving reference frame, we use a pseudo-spectral method⁴⁶ to solve the nondimensionalized LL equation, Eq. (1). Here, the localized, perpendicular field moves with velocity \bar{V} while the fluid velocity is zero. The simulation domain in this case has the same size as the simulations in the static reference frame but it is discretized into the coarser 256×128 number of grid points by virtue of the accuracy of the pseudo-spectral method. We initialize the simulation with a homogeneous magnetization with $\bar{n} = h_0 = 0.7$, $\bar{u} = 0$ and use periodic boundary conditions along and across the thin film. We evolve the simulation to $t = 2000$. The longer simulation time in this case reflects the slower dynamics in the moving reference frame. The value of the homogeneous perpendicular field bias magnitude, h_0 , was chosen to minimize the strength of the localized perpendicular field needed to impose hydrodynamic vacuum.

The phase space for the nucleated nonlinear structures and dynamics as a function of \bar{V} and d is shown in Fig. 6(a), swept in steps of 0.1 and 1, respectively. As in Fig. 3(a), subsonic laminar flow (region O) is lost as the obstacle diameter increases. Regions I to III denote V-AV pair nucleation. In contrast to the static reference frame, the absence of underlying fluid velocity in this case, $\bar{u} = 0$, precludes a significant vortex translation or Kelvin motion. Instead, the V-AV pairs are attracted to each other due to magnetic damping (energy dissipation) and subsequently annihilate, expelling spin waves. For this reason, the V-AV pairs nucleated at subsonic conditions (region I) are unstable and lead to an unevenly spaced V-AV train as well as irregular dynamics close to the obstacle, Fig. 6(b). At supersonic conditions, above

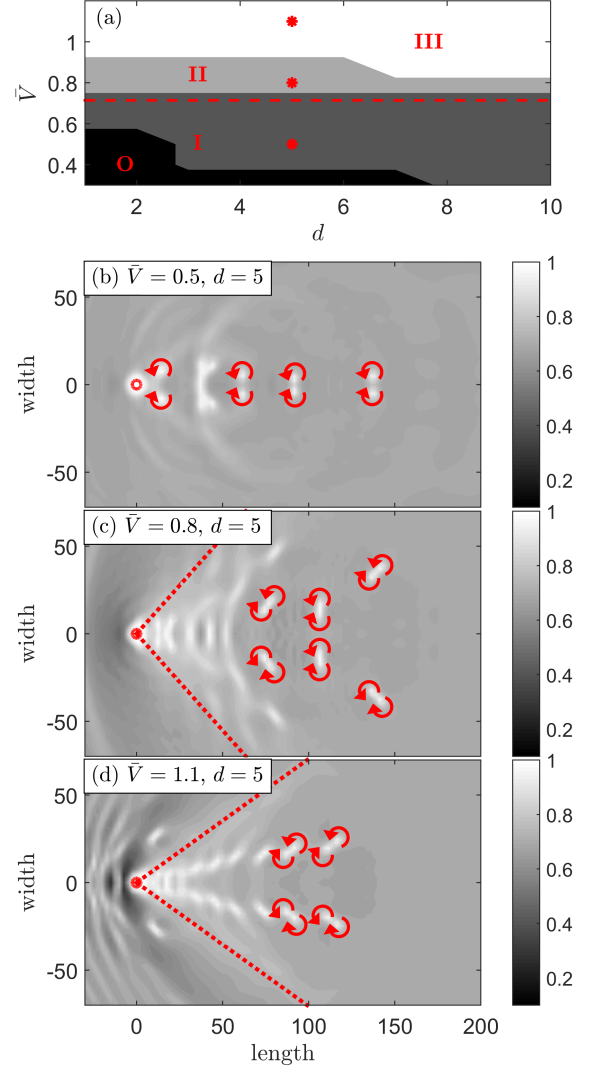


FIG. 6. (color online) (a) Phase diagram for V-AV nucleation and dynamics in the moving reference frame. Region O represents laminar flow, where vortices are not nucleated. The gray regions I-II (region III) denote irregular (ordered) V-AV pair nucleation. Snapshots of the longitudinal spin density, n , show V-AV (b) annihilation (region I), (c) irregular dynamics (region II) and (d) ordered dynamics (region III) inside the Mach cone with conditions indicated by red asterisks in (a). The red arrows represent the vortices' circulation direction.

the red dashed line in Fig. 6(a), a narrow phase space (region II) leads to irregular V-AV pairs inside the Mach cone, shown in Fig. 6(c) by red dashed lines calculated from Eq. (19b). Finally, in region III, the V-AV pairs become mostly ordered. In Fig. 6(d) we observe two V-AV pairs establishing an oblique path with respect to the obstacle. This is reminiscent of oblique solitons³⁷, but here the structure immediately breaks down into V-AV pairs.

As discussed above, a Mach cone and wavefronts are also established at supersonic conditions in the moving reference frame. These agree to good accuracy with

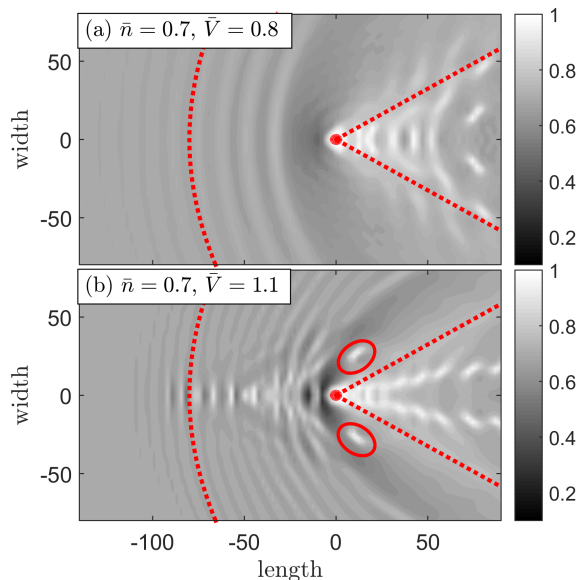


FIG. 7. (color online) Snapshots of the longitudinal spin density, n , in the moving reference frame at supersonic conditions. The moving localized field has a diameter $d = 5$. The Mach cone calculated from Eq. (19a) and the wavefront calculated from Eq. (21a) are shown by red dashed lines. Instabilities in the wavefronts lead to V-AV pairs, red circles.

Eqs. (19b) and (21), where the curves of constant phase for x and y , analogous to Eq. (22), are determined as in Ref. 36. Figure 7 shows the comparison between theory and numerics. However, we observe instabilities in the wavefronts that develop for large obstacle velocities. This is shown in Fig. 7(a) and (b) for, respectively, velocities similar and larger than the sonic curve. In particular, the short wavefronts in Fig. 7(b) are observed to break into V-AV pairs due to this instability (encircled in red) suggesting nonlinear effects. The study of such effects are outside the scope of the current manuscript.

VI. CONCLUSION

In summary, we demonstrate that nonlinear structures and V-AV complexes can be nucleated from an obstacle in a thin film planar ferromagnet. These observations are in qualitative agreement with structures nucleated in fluids and superfluids, providing further evidence for the hydrodynamic properties of thin film planar ferromagnets.

Both in the moving and static reference frames, we observe nucleation of V-AV pairs, as qualitatively expected for an unsteady wake formed behind an impenetrable obstacle. These V-AV pairs experience diverse dynamics and are nucleated as long as the system is out of equi-

librium. In the static reference frame, we observe Kelvin motion, instability, and V-V, AV-AV rotation. In the moving reference frame, V-AV pairs are also nucleated but generally annihilate, forming an irregular pattern and spin waves. For supersonic conditions, a Mach cone and the formation of wavefronts are observed, as expected for superfluids. Good quantitative agreement is found between the numerically observed structures and theoretical results derived from the linearized, conservative, long-wave equations.

Although nonlinear structures and V-AV complexes are observed in both the static and moving reference frames, there are important differences in their dynamics. In particular, irregular V-AV dynamics are observed in supersonic conditions in the static reference frame, $\bar{u} > 0$ and $\bar{V} = 0$, and subsonic conditions in the moving reference frame, $\bar{u} = 0$ and $\bar{V} > 0$. This is due to the fact that the underlying flow, $\bar{u} \neq 0$, induces V-AV translation in contrast to the moving reference frame with $\bar{u} = 0$. In other words, a topological texture is required to support ordered vortex structures. This suggests that for a fixed $\bar{u} > 0$ the introduction of $\bar{V} \neq 0$ leads to irregularity in the subsonic regime. Additionally, the numerical observation of an apparently stable V-AV train propagating on the textured background $\bar{u} > 0$ is to be contrasted with the unstable propagation of a train of counter-rotating vortices in a BEC. This intriguing ordered regime requires further analysis.

It is noteworthy that we explore a two-dimensional parameter space with a fixed \bar{u} in the static reference frame and a fixed \bar{n} in the moving reference frame, as opposed to the full three-dimensional parameter space where \bar{n} , d , and \bar{u} or \bar{V} are varied. However, we argue that the phase spaces shown in Fig. 3(a) and Fig. 6(a) represent general qualitative features of the full parameter space. The phase space can collapse to two dimensions, spanning $M_u = M_u(\bar{n}, \bar{u})$ or $M_V = M_V(\bar{n}, \bar{V})$ versus d . Micromagnetic simulations performed with several choices of \bar{n} and \bar{u} and \bar{V} for, respectively, the static and moving reference frames, indeed return qualitatively similar dynamics for matching Mach numbers and obstacle diameters.

The above results show that V-AV complexes can be nucleated in a thin film ferromagnet with planar anisotropy following well-defined patterns analogous to super and compressible fluids. Our observations are relevant for the stability of spin-density waves and the study of V-AV interactions with other nonlinear textures such as spin-density waves, other V-AV pairs, and wavefronts.

ACKNOWLEDGMENTS

E.I. acknowledges support from the Swedish Research Council, Reg. No. 637-2014-6863. M.A.H. partially supported by NSF CAREER DMS-1255422.

-
- * ezio.iacocca@colorado.edu
- ¹ J. Stör and H. C. Siegmann, *Magnetism: from fundamentals to nanoscale dynamics* (Springer, 2006).
 - ² A. Hubert and R. Schäfer, *Magnetic domains: the analysis of magnetic microstructures* (Springer, 2009).
 - ³ W. Tong, M. Wu, L. D. Carr, and B. A. Kalinikos, Phys. Rev. Lett. **104**, 037207 (2010).
 - ⁴ Z. Wang, M. Cherkasskii, B. A. Kalinikos, L. D. Carr, and M. Wu, New Journal of Physics **16**, 053048 (2014).
 - ⁵ M. A. Hoefer, T. J. Silva, and M. W. Keller, Phys. Rev. B **82**, 054432 (2010).
 - ⁶ S. M. Mohseni, S. R. Sani, J. Persson, T. N. A. Nguyen, S. Chung, Y. Pogoryelov, P. K. Muduli, E. Iacocca, A. Eklund, R. K. Dumas, S. Bonetti, A. Deac, M. A. Hoefer, and J. Åkerman, Science **339**, 1295 (2013).
 - ⁷ E. Iacocca, R. K. Dumas, L. Bookman, M. Mohseni, S. Chung, M. A. Hoefer, and J. Åkerman, Phys. Rev. Lett. **112**, 047201 (2014).
 - ⁸ F. Macià, D. Backes, and A. Kent, Nature Nanotechnol **10**, 1038 (2014).
 - ⁹ S. Chung, A. Eklund, E. Iacocca, S. Mohseni, S. Sani, L. Bookman, M. A. Hoefer, R. Dumas, and J. Åkerman, Nature Communications **7** (2016).
 - ¹⁰ N. Romming, C. Hanneken, M. Menzel, J. E. Bickel, B. Wolter, K. von Bergmann, and R. Kubetzka, A. Wiesendanger, Science **341**, 636 (2013).
 - ¹¹ J. Sampaio, V. Cros, S. Rohart, A. Thiaville, and A. Fert, Nature Nanotechnology **8**, 839 (2013).
 - ¹² Y. Zhou, E. Iacocca, A. Awad, R. Dumas, H. Zhang, H. B. Braun, and J. Åkerman, Nature Communications **6** (2015).
 - ¹³ W. Jiang, P. Upadhyaya, W. Zhang, G. Yu, M. B. Jungfleisch, F. Y. Fradin, J. E. Pearson, Y. Tserkovnyak, K. L. Wang, O. Heinonen, S. G. E. te Velthuis, and A. Hoffmann, Science **349**, 283 (2015).
 - ¹⁴ J. König, M. C. Bønsager, and A. H. MacDonald, Phys. Rev. Lett. **87**, 187202 (2001).
 - ¹⁵ E. B. Sonin, Advances in Physics **59**, 181 (2010).
 - ¹⁶ S. Takei and Y. Tserkovnyak, Phys. Rev. Lett. **112**, 227201 (2014).
 - ¹⁷ H. Chen, A. D. Kent, A. H. MacDonald, and I. Sodemann, Phys. Rev. B **90**, 220401 (2014).
 - ¹⁸ E. Iacocca, T. J. Silva, and M. A. Hoefer, Phys. Rev. Lett. **118**, 017203 (2017).
 - ¹⁹ B. Halperin and P. Hohenberg, Physical Review **188**, 898 (1969).
 - ²⁰ C. Pethick and H. Smith, *Bose-Einstein condensation in dilute gasses* (Cambridge University Press, 2002).
 - ²¹ G. A. El and M. A. Hoefer, Physica D Dispersive Hydrodynamics, **333**, 11 (2016).
 - ²² D. M. Stamper-Kurn and M. Ueda, Rev. Mod. Phys. **85**, 1191 (2013).
 - ²³ C. Qu, L. P. Pitaevskii, and S. Stringari, Phys. Rev. Lett. **116**, 160402 (2016).
 - ²⁴ T. Congy, A. M. Kamchatnov, and N. Pavloff, SciPost Phys. **1**, 006 (2016).
 - ²⁵ K. Yamada, S. Kasai, Y. Nakatani, K. Kobayashi, H. Kohno, A. Thiaville, and T. Ono, Nature **6**, 269 (2007).
 - ²⁶ G. Beach, M. Tsoi, and J. Erskine, Journal of Magnetism and Magnetic Materials **320**, 1272 (2008).
 - ²⁷ M. Yan, A. Kákay, C. Andreas, and R. Hertel, Phys. Rev. B **88**, 220412 (2013).
 - ²⁸ C. H. K. Williamson, Annual Review of Fluid Mechanics **28**, 477 (1996).
 - ²⁹ T. Lewke, S. Le Dizès, and C. H. K. Williamson, Annual reviews of Fluid Mechanics **48**, 506 (2016).
 - ³⁰ M. T. Reeves, T. P. Billam, B. P. Anderson, and A. S. Bradley, Phys. Rev. Lett. **114**, 155302 (2015).
 - ³¹ T. Frisch, Y. Pomeau, and S. Rica, Phys. Rev. Lett. **69**, 1644 (1992).
 - ³² C. Nore, M. Brachet, and S. Fauve, Physica D: Nonlinear Phenomena **65**, 154 (1993).
 - ³³ K. Sasaki, N. Suzuki, and H. Saito, Phys. Rev. Lett. **104**, 150404 (2010).
 - ³⁴ W. J. Kwon, J. H. Kim, S. W. Seo, and Y. Shin, Phys. Rev. Lett. **117**, 245301 (2016).
 - ³⁵ I. Carusotto, S. X. Hu, L. A. Collins, and A. Smerzi, Phys. Rev. Lett. **97**, 260403 (2006).
 - ³⁶ Y. G. Gladush, G. A. El, A. Gammal, and A. M. Kamchatnov, Phys. Rev. A **75**, 033619 (2007).
 - ³⁷ G. A. El, A. Gammal, and A. M. Kamchatnov, Phys. Rev. Lett. **97**, 180405 (2006).
 - ³⁸ R. Hertel and C. M. Schneider, Phys. Rev. Lett. **97**, 177202 (2006).
 - ³⁹ K. Everschor-Sitte, M. Sitte, T. Valet, J. Sinova, and A. Abanov, arXiv:1610.08313 (2016).
 - ⁴⁰ N. Papanicolaou and T. Tomaras, Nuclear Physics B **360**, 425 (1991).
 - ⁴¹ R. Balakrishnan, I. I. Satija, and C. W. Clark, Phys. Rev. Lett. **103**, 230403 (2009).
 - ⁴² C. P. Rubbo, I. I. Satija, W. P. Reinhardt, R. Balakrishnan, A. M. Rey, and S. R. Manmana, Phys. Rev. A **85**, 053617 (2012).
 - ⁴³ N. Papanicolaou and P. N. Spathis, Nonlinearity **12**, 285 (1999).
 - ⁴⁴ R. Courant and K. O. Friedrichs, *Supersonic flow and shock waves* (Springer Berlin, 1948).
 - ⁴⁵ A. Vansteenkiste, J. Leliaert, M. Dvornik, M. Helsen, F. Garcia-Sanchez, and B. Van Waeyenberge, AIP Advances **4**, 107133 (2014).
 - ⁴⁶ M. Hoefer and M. Sommacal, Physica D: Nonlinear Phenomena **241**, 890 (2012).